Heat and Mass Transfer
https://doi.org/10.1007/s00231-021-03104-y

ORIGINAL ARTICLE

Pumping power and heating area dependence of thermal resistance for a large-scale microchannel heat sink under extremely high heat flux

Bo Sun[1] · Huiru Wang[2] · Zhongshan Shi[3] · Ji Li[4]

Received: 1 March 2021 / Accepted: 18 June 2021

Abstract
In this paper, based on the Li-Peterson pumping consumption-thermal resistance optimization model, a single-phase structure-optimized large-scale microchannel heat sink with each channel having 0.2 mm width and 0.8 mm height for extremely high heat flux cooling was proposed and investigated. Employing deionized water as coolant, two different heat source areas were designed and the results were compared under different pumping power from 0.1 W to 6.5 W. The experimental and simulation results indicates that the proposed copper-based microchannel thermal management system can dissipate heat flux of 1000 W/cm^2 over 1cm^2 and 500 W/cm^2 over 5cm^2, respectively, adding critical data support to the database of single-phase microchannel heat sink with heat removal capacity exceeding 1000 W/cm^2. Moreover, the possible minimum thermal resistance over a broad pumping power range of 0.1 W to 6.5 W was explored. Extremely low thermal resistance of 0.065 K/W and 0.019 K/W were obtained for these two heating area scenarios. Overall, the proposed copper-based optimized microchannel heat sink is an ideal solution to cool high heat flux devices.

Nomenclature

A_{ch}	Effective heat transfer area (m^2)
A_{hs}	Source dimension (m^2)
c_p	Specific heat capacity (J/(kg•K))
D_h	The characteristic dimension of microchannel (m)
D_{tube}	The inner diameter of tube (m)
f	Fanning friction factor
f_{app}	Apparent friction factor
G	Flow rate (L/h)
h	Convective heat transfer coefficient (W/(m^2•K))
H	Height of channel (mm)
H_b	Thickness of microchannel substrate (mm)
I	Current (A)
K_w	Thermal conductivity of deionized water (W/(m•K))
L	Length of channel (mm)
m	Mass flow (kg/s)
N	Number of microchannels
Nu	Nusselt number
P	Pressure (kPa)
P_w	Pumping power (W)
P_Q	Input heating power by AC power (W)
ΔP	Pressure drop (kPa)
Pr	Prandt number
Q	Heating power (W)

Highlights

- A structure-optimized large microchannel heat sink for extremely high heat flux was designed.
- Rough surface promotes heat transfer through creating flow disturbance at low Re number.
- Actual heat fluxes of 1104.54W/cm^2 and 480.60W/cm^2 were dissipated over 1cm^2 and 5cm^2 area.
- Dependence of thermal resistance on pumping power between 0.1W and 6.5W was identified.
- Unprecedented low thermal resistance of 0.065K/W and 0.019K/W were obtained respectively.

✉ Ji Li
jili@ucas.ac.cn

1 School of Engineering Science, University of Chinese Academy of Sciences, 19A Yu-quan-lu Road, Shijingshan District, Beijing 100049, PR China

2 School of Mechanical Engineering, Shenyang University of Technology, Shenyang 110870, China

3 Dawning Information Industry Co., LTD, Beijing, China

4 Laboratory of Advanced Thermal Management Technologies, School of Engineering Science, University of Chinese Academy of Sciences, 19A Yu-quan-lu Road, Shijingshan District, Beijing 100049, PR China

Published online: 01 July 2021

q	Heat flux (W/cm^2)
R	Total thermal resistance of heat sink (K/W)
R_{cd}	Conduction thermal resistance of heat sink (K/W)
R_{cv}	Convection thermal resistance of heat sink (K/W)
R_c	Capacity thermal resistance of heat sink (K/W)
Re	Reynolds number
T	Temperature (°C)
T_{hs}	Junction temperature of heat sink (°C)
T_m	Mean temperature (°C)
T_a	Ambient temperature (°C)
ΔT	Temperature difference (°C)
U	Voltage (V)
u	Velocity (m/s)
W	Width of channel (mm)
μ	Viscosity (kg/(m•s))
ρ	Density (kg/m^3)
MEMS	Micro electro mechanical systems
DC	Direct current
AC	Alternating current
ch	Microchannel
hs	Heat sink
in/inlet	Inlet
out/outlet	Outlet

1 Introduction

The heat fluxes of devices such as high-performance computer chips, lasers and nuclear reactor are rapidly increasing, and the problem of heat accumulation and overheating is getting deteriorate [1]. In recent decades, the heat flux of the chip has reached 500 W/cm^2 in the field of Micro-Electro-Mechanical Systems (MEMS), and the local hot spot can exceed 1000 W/cm^2 [2–5]. For instance, the thermal flux of the next generation of IGBT modules will gradually increase from 100 W/cm^2 to 500 W/cm^2 [6]. For high-power laser devices, each diode laser needs to dissipate 500 W/cm^2 of heat flux while keeping the operating temperature as low as possible [7]. In the nuclear power engineering, the heat flux generated by components included in fusion reactors and defense applications can be up to 10^4 W/cm^2 [8].

Generally, the operating temperature of electronic devices should be less than 85 °C, and the reliability of products will be decreased by 50% if over-heated temperature exceeding 10 °C [9–11]. Since the demand of miniaturized design also limits the heat dissipation space, the uneven internal temperature distribution and poor heat dissipation have a series of negative effects, which will ultimately affect the performance and reliability of electronic devices. Therefore, reasonable thermal management is critical to electronic products [12, 13].

Current cooling technologies mainly include air cooling, liquid cooling, heat pipe, micro structure and spray cooling. As proposed by previous works, the traditional cooling method has relatively limited heat dissipation capacity, while the microchannel liquid cooling can handle a heat dissipation load of more than 1000 W/cm^2 [14–16], which is expected to meet the urgently demand for high heat flux cooling in the near future.

The concept of microchannel cooling technology was first introduced in the previous experimental study of Tuckerman and Pease in 1980s [17]. Due to micrometer size and large surface area to volume ratio, efficiently heat transfer can be obtained and the heat flux of 790 W/cm^2 was dissipated. Since then, owing to unique features of microchannel [18], the flow and heat transfer characteristics of microchannel under high heat flux have been extensively explored.

Skidmore et al. [19] proposed a laser diode array cooled by silicon monolithic microchannel. Up to 1.5 kW/cm^2 is achieved continuous wave at an emission wavelength of ~ 808 nm, and the continuous wave thermal resistance of the 10 bar diode array is 0.032 °C/W. Qu and Mudawar [20] investigated the pressure drop and heat transfer characteristics of a single-phase microchannel heat sink both experimentally and numerically. Using rectangular microchannel, the maximum heat flux dissipated in the experiment was 200 W/cm^2 with 86 kPa. Chang et al. [21] designed and tested a microchannel heat exchanger fabricated directly on the back of the chip. The results showed that under non-uniform heating conditions, microchannel with a width of 61 μm and a depth of 272 μm could obtain the best thermal resistance of 0.09($K{\cdot}cm^2$)/W and sustain the highest heat flux of 1250 W/cm^2. In order to evaluate the practical application potential of mini/micro-channel radiators for high heat flux cooling, two samples of mini/micro-channel cooling loop were established and tested by Hirshfeld et al. [22]. The results showed that both structures could achieve high heat flux in the range of 500 W/cm^2. Solovitz et al. [23] conducted experiments to study the trapezoidal copper microchannel heat sink for cooling high-power equipment. The thermal resistance of the cooler was 0.15($K{\cdot}cm^2$/W), and the thermal performance was better than existing radiator. Brunschwiler et al. [24] tested the ability of parallel plates, microchannels, needle fins, linear and staggered structures to dissipate heat from a 1cm^2 chip heat source area. Using straight pin fins, with 200 μm and 100 μm pitch and 100 μm and 200 μm height, cooler could remove heat flux of 177 W/cm^2 and 186 W/cm^2, respectively. A high-performance ultra-thin manifold heat sink composed of jet and microchannel was proposed by Escher et al. [25]. With the hydraulic diameter of 35-80 μm, the microchannel heat sink proposed by

Koyuncuoğlu et al. [26] was able to absorb 127 W/cm^2 heat flux from hot spot and 50 W/cm^2 from the remaining heated surface. The microchannel cooler proposed by Kozłowska et al. [27] was able to cooling high power diode laser arrays at heat flux range from 200 W/cm^2 to 380 W/cm^2.

In addition, many methods for enhancing flow and heat transfer in microchannel heat sinks have been further discussed [28–36]. Colgan et al. [28] described a practical implementation of micro-channel cooler with staggered and continuous fins designed for cooling ultra-high power chips such as microprocessors. Coolers of this design achieved chip cooling with power densities of 400 W/cm^2 and kept fluid pressure drop less than 35 kPa. Lee et al. [29] applied oblique fin microchannel heat sinks to alleviate the hot spots generated on the silicon chip with heat flux of 400 W/cm^2, which effectively improved the temperature uniformity of the chip. Xia et al. [30] studied the characteristics of temperature variation and pressure drop in the compound corrugated microchannel radiator by experiment, in which the maximum heat flux was 200 W/cm^2. Both Liu et al. [31] and Zhang et al. [32] used galinstan as cooling fluid exploring the heat transfer potential in minichannel and T-Y-type microchannel respectively, with maximum heat flux of 140 W/cm^2 and 300 W/cm^2. Shamim et al. [33] proposed a scheme using microchannel to cooling 3D multicore chips, and studied it from three aspects: pressure drop, flow rate and heat transfer efficiency. With 0.05 W pumping power of the system, the heat dissipation of 200 W/cm^2 has been demonstrated. Xie et al. [34] investigated the pressure drop and heat transfer features of a microchannel applying staggered diamond micro-pin fins. Using visualization experiments, the mechanism of heat transfer were discussed. Yang et al. [35] proposed a novel optimization approach and a hybrid design using manifold arrangement and secondary channels for microchannel heat sink. The results indicate that the hybrid heat sink can simultaneously reduce the thermal resistance and pressure drop. More recently, Erp et al. [36] produced a monolithically integrated manifold microchannel cooling structure which withstands heat fluxes exceeding 1700 W/cm^2 using only 0.57 W/cm^2 of pumping power.

From relevant experimental studies mentioned above, it is evident that single-phase microchannel structures have great heat transfer potential which worthy of further exploring. From historical literature review, it is found that: (i) the experimental studies of single-phase microchannel cooling which heat flux exceeding 1000 W/cm^2 are very limited and the heat source is generally less than 1cm^2, which cannot meet the large heating area and ultra-high heat flux demands, such as, IGBT and nuclear fusion facilities [37]; (ii) the thermal resistance under different pumping power conditions has not been well addressed, especially under high pumping power; (iii) before taking the ways to reduce the pressure drop along the microchannel heat sink (e.g., using manifold structures), the possible potential of microchannel heat sinks has not yet been identified, especially adopting the optimization of the structure.

The purpose of this study is to explore the heat transfer potential of a large-scale microchannel heat sink with an optimized structure based on our early established model of minimization of thermal resistance versus pump power under different conditions of high heat flux, heat area, and pumping power. Considering the comprehensive influence of pump power, heating area, and heat flux density on the thermal resistance of microchannel heat sinks, there are still lacking of such kind of historical work according to the author's knowledge. The ultimate the goal of our research on large-scale microchannel heat sinks is to provide practical and efficient cooling methods for large-scale and high heat flux equipment, such as high-power laser arrays and nuclear fusion reactors.

In this work, based on the Li-Peterson pumping power consumption-thermal resistance minimization model [38, 39], a large-scale microchannel heat sink is designed and fabricated with microchannel dimensions close to its optimized structure, of which rough surface was created along the microchannels through micromachining and etching process. The temperature variations and pressure drop along the single-phase microchannel heat sink were carefully measured and compared with the numerical simulation of turbulent heat transfer model. Two kinds of heat source areas (1cm^2 and 5cm^2) are selected to study the hydraulics and thermal characteristics of microchannel heat sink with extremely high heat flux more than 500 W/cm^2 over 5cm^2 and 1000 W/cm^2 over 1cm^2 under very wide range of pumping power from 0.1 W-6.5 W, which was not revealed and compared before according to the authors' knowledge. The experimental results add critical data support to the database of single-phase microchannel heat sink with heat removal capacity exceeding 1000 W/cm^2 and explored the possible lowest thermal resistance over a broad pumping power range of 0.1 to 6.5 W.

2 Experimental apparatus

2.1 Heat sink fabrication and assembly

The experimental device diagram of a high-power cooling cycle system is shown in the Fig. 1(a). The cooling system is divided into three parts: the water circulation system, the data collection system and the test section.

The water circulation system consists of thermostatic water tank, miniature water pump, filter, electronic flowmeter, valve, liquid-to-air heat exchanger, and fans. The electronic flow meter with a measurement range of 0.1–0.6m^3/h and an accuracy of 0.5% was used to measure the real-time

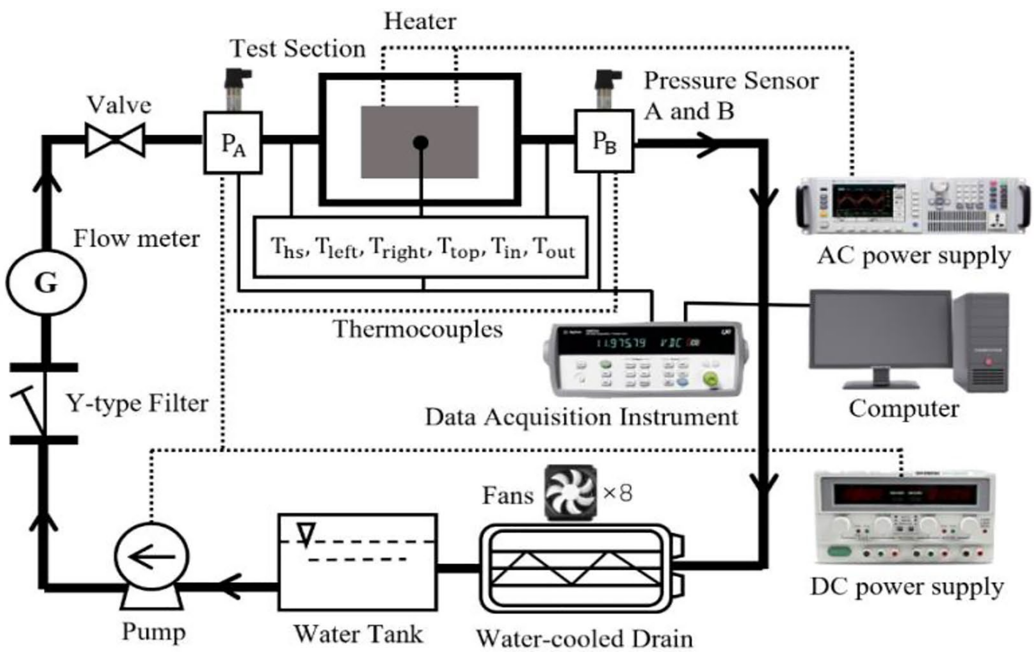

(a) The cooling loop.

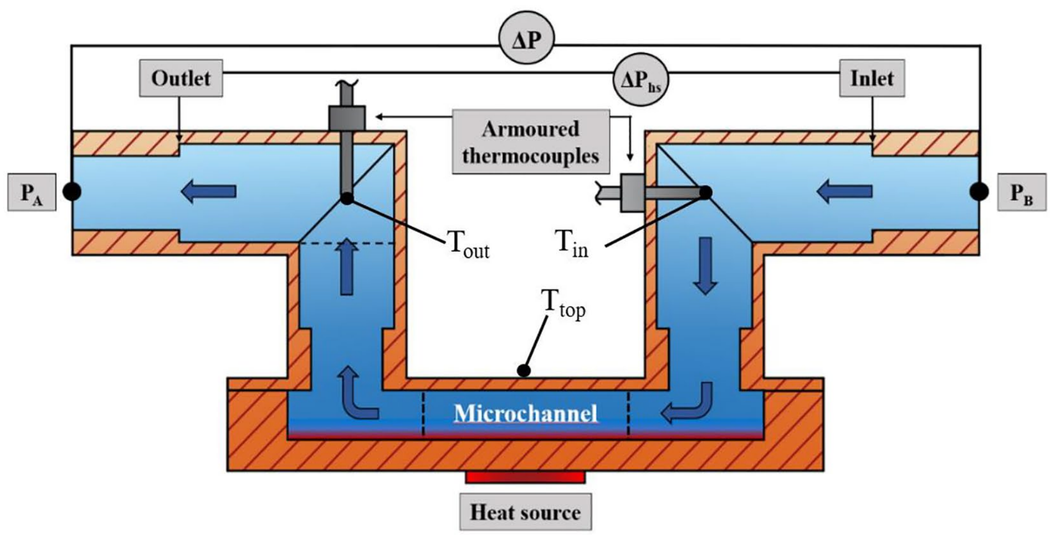

(b) The locations of the pressure and temperature sensors on the microchannel heat sink.

Fig. 1 Schematic diagram of the experimental setup

volume flow of the circulating system. The deionized water subsequently entered the test section. After heated, the hot water flowed out of the heat sink and entered the liquid-to-air heat radiators. Eight 120 mm fans (each with a rated voltage of 12 V) were used to cool the radiators. Finally, the coolant returned to the tank and the inlet water temperature maintained at 25 oC. During the whole testing, the ambient temperature was maintained at about 25 ± 1 °C.

The data acquisition system included pressure sensors, thermocouples, an Agilent data acquisition system and a computer. Pressure sensors were arranged on both sides of the microchannel heat sink to measure the inlet and outlet pressure of the test section. The range of pressure sensor are 0 ~ 5PSIG and 0 ~ 50PSIG (OMEGA PX409-005 and PX409-050), and the measurement accuracy is 0.08%. As shown in the Fig. 1(b), two armored T-type thermocouples were installed at the inlet and outlet of heat sink to measure the change of coolant temperature. In addition, shown in Fig. 2, three T-type thermocouples were installed at different positions of the microchannel heat sink. T_{top} was located at the center point of the upper cover, the T_{left} and T_{right} were 5 mm away from the center of the base plate. T_{hs} was located at the center point of the top surface of the heating block. The accuracy of OMEGA T-type thermocouples are ± 0.2 °C. All data were collected by the data acquisition instrument (Agilent 34970A with a measurement error of ± 0.1 °C).

The test section consists of a microchannel heat sink, a heating block and AC power supplies. During the experiment, the power input for the heating block was controlled by adjusting the AC power supplies. The heating block consists of two parts: the copper block and the cartridge heaters (each cartridge heater has a diameter of 10 mm, a length of 80 mm, and a rated power of 300 W). The copper block welded with the cartridge heaters was served as the heat source, and the total power of 10 cartridge heaters can reach 3000 W. To minimize the contact thermal resistance, the bottom surface of the heat sink substrate was tightly connected with the heating block by a thin layer tin soldering to fill the air gap. Stainless steel plates and bolts were used to fasten the test section. Two heating area cases were designed, as shown in Fig. 2, which were 10 mm × 10 mm and 50 mm × 10 mm, respectively. In order to minimize the heat loss from the surface of test section to the ambient, a layer of insulation cotton (thermal conductivity about 0.032 W/(m·K) at 25 °C) with 6 mm thick was used to wrap the surface of test piece.

The microchannel heat sink with each channel having 200 microns width and 800 microns height was fabricated. Furthermore, scanning electron micrographs (SEM) of the microchannels are also shown in Fig. 3. A high voltage wire cutting process as selected as the processing method in this work, other than etching or skiving fabrication. The purpose of high voltage wire cutting is to generate very rough inner surface to produce small perturbation in microchannel flow under comparatively low Reynolds number. After machining process, the microchannel heat sink was further developed in high concentration hydrochloric acid. Such an extra corrosion process is to increase the roughness of the microchannel surface. The typical roughness from Fig. 3 can be determined around 5 microns ~ 10 microns. This roughness cannot be ignored compared to 200 microns channel width.

3 Data processing and analysis

3.1 Flow Characteristics

The pressure drop in microchannel associated with apparent friction factor f_{app} can be expressed as

$$\Delta P_{ch} = \frac{2 f_{app} \rho u_{ch}^2 L}{D_h} \tag{1}$$

where L is the length of microchannel; D_h is the hydraulic diameter, expressed as followed:

$$D_h = \frac{4WH}{2(W+H)} \tag{2}$$

where W is the width of microchannel, and H is the height of microchannel.

In the experimental process, the velocity can be calculated by measuring the flow rate, so the friction coefficient can be calculated by measuring the pressure drop and flow rate. At the same time, according to the definition of Reynolds number, the relationship between friction coefficient and Reynolds number can be further discussed,

$$\mathrm{Re} = \frac{u_{ch} D_h}{\nu} \tag{3}$$

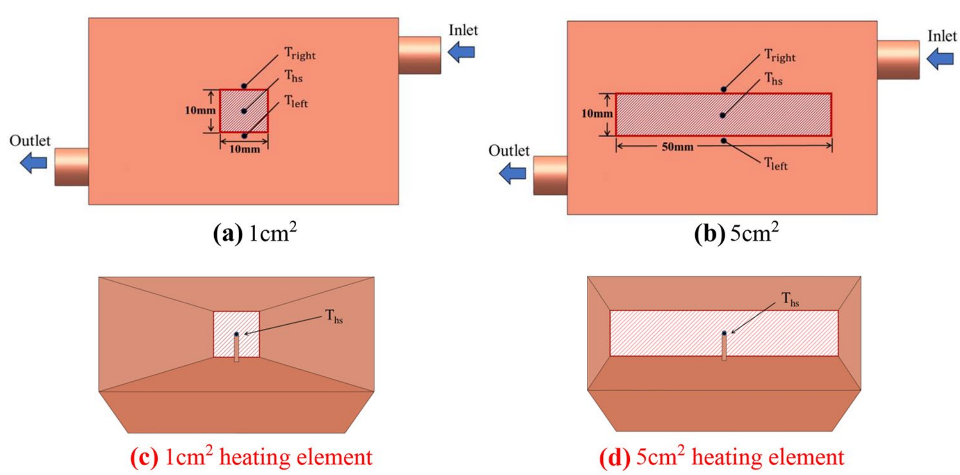

Fig. 2 Schematic diagram of heating zone and heating elements

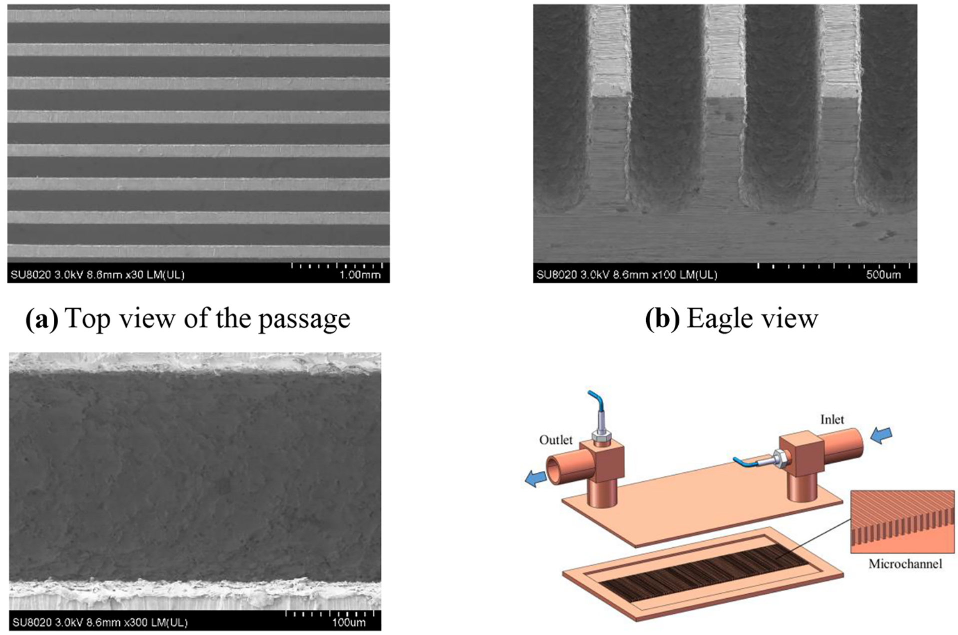

(a) Top view of the passage **(b)** Eagle view

(c) Rough surface of the microchannel **(d)** Schematic diagram of heat sink

Fig. 3 SEM pictures and schematic diagram of microchannels

$$\mathrm{Re} = \frac{u_{ch} D_h}{\nu}$$

where ν is the kinematic viscosity. In the calculation process, the thermo-physical parameters such as the density and dynamic viscosity coefficient of the fluid are calculated based on T_m which is expressed as following:

$$T_m = \frac{T_{in} + T_{out}}{2} \tag{4}$$

Where T_{in} and T_{out} are the temperature of inlet and outlet.

3.2 Heat Transfer

The analysis of heat transfer characteristics of microchannels is mainly focused on the study of convective heat transfer coefficient and Nu number. When the fluid passes through the microchannel, the heat transferred by the heating block was obtained. Electrical heating power was controlled by adjusting the voltage of AC power supply. The formula for calculating heating power is as follow,

$$P_Q = U \cdot I \tag{5}$$

The formula for heat transfer by coolant is as follow

$$Q = c_p m \Delta T \tag{6}$$

Where P_Q is heating power, U is voltage of AC power supply, I is current of AC power supply, c_p is specific heat capacity of water, m is mass flow of water, ΔT is temperature difference between import and export water. In the absence of heat loss, the results from Eq. (5) and (6) should be same.

The effective heat transfer coefficient h is expressed as

$$h = \frac{Q}{A_{ch} \cdot (T_{hs} - T_m)} \tag{7}$$

where Q is the real input heat load from Eq. (6); A_{ch} is effective heat transfer area of the microchannel heat sink as following:

$$A_{ch} = (2HL_{heat} + 2WL_{heat}) \cdot N \tag{8}$$

where W and H are the width and height of microchannels; L_{heat} is the length of the microchannel involved in heat transfer; N is the number of channel to be heated.

Nusselt number can be calculated as:

$$Nu = \frac{hD_h}{k_w} \tag{9}$$

where k_w is the thermal conductivity of deionized water.

3.3 Thermal performance

The total thermal resistance of heat sink R was divided into three components: conduction thermal resistance R_{cd} convection thermal resistance, R_{cv} and capacity thermal resistance R_{cv}

$$R = R_{cd} + R_{cv} + R_c \tag{10}$$

$$R = \frac{T_{hs} - T_{in}}{Q} \tag{11}$$

$$R_{cd} = \frac{H_b}{k_{cu} A_{hs}} \tag{12}$$

$$R_{cv} = \frac{T_{hs} - T_m}{Q} - R_{cd} = \frac{1}{hA_{hs}} \tag{13}$$

$$R_c = \frac{T_m - T_{in}}{Q} \tag{14}$$

where H_b is the thickness of microchannel substrate, k_{cu} is the thermal conductivity of copper, and A_{hs} is the area of heat source.

3.4 Uncertainty analysis

Uncertainty analysis for each parameter is summarized in Tab. 1, respectively:

4 Turbulent heat transfer model of microchannel heat sink

The computational domain according to the experimental microchannel heat sink is shown in Fig. 4. The pressure sensors arranged on inlet and outlet of the microchannel heat sink were ignored to simplify the model.

The three dimensional turbulent flow and heat transfer processes were numerically solved with the following assumptions: (1) the heat transfer fluid is single phase, Newtonian and incompressible; (2) both fluid flow and heat transfer are in steady state; (3) the radiation heat transfer, body force and dissipating heat caused by viscosity are neglected. According to the above assumptions, the governing equations of continuity, momentum and energy for liquid can be established as follows.

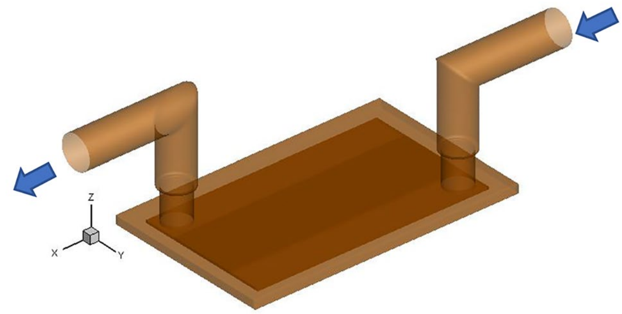

Fig. 4 Computational domain of the microchannel heat sink

Continuity equation:

$$\frac{\partial(\rho u)}{\partial x} + \frac{\partial(\rho v)}{\partial y} + \frac{\partial(\rho w)}{\partial z} = 0$$

Momentum equation:

$$\frac{\partial(\rho uu)}{\partial x} + \frac{\partial(\rho uv)}{\partial y} + \frac{\partial(\rho uw)}{\partial z} = -\frac{\partial P}{\partial x} + \frac{\partial}{\partial x}\left[(\mu+\mu_t)\left(\frac{\partial u}{\partial x} + \frac{\partial u}{\partial x}\right)\right] + \frac{\partial}{\partial y}\left[(\mu+\mu_t)\left(\frac{\partial u}{\partial y} + \frac{\partial v}{\partial x}\right)\right] + \frac{\partial}{\partial z}\left[(\mu+\mu_t)\left(\frac{\partial u}{\partial z} + \frac{\partial w}{\partial x}\right)\right]$$

$$\frac{\partial(\rho vu)}{\partial x} + \frac{\partial(\rho vv)}{\partial y} + \frac{\partial(\rho vw)}{\partial z} = -\frac{\partial P}{\partial y} + \frac{\partial}{\partial x}\left[(\mu+\mu_t)\left(\frac{\partial v}{\partial x} + \frac{\partial u}{\partial y}\right)\right] + \frac{\partial}{\partial y}\left[(\mu+\mu_t)\left(\frac{\partial v}{\partial y} + \frac{\partial v}{\partial y}\right)\right] + \frac{\partial}{\partial z}\left[(\mu+\mu_t)\left(\frac{\partial v}{\partial z} + \frac{\partial w}{\partial y}\right)\right]$$

$$\frac{\partial(\rho wu)}{\partial x} + \frac{\partial(\rho wv)}{\partial y} + \frac{\partial(\rho ww)}{\partial z} = -\frac{\partial P}{\partial z} + \frac{\partial}{\partial x}\left[(\mu+\mu_t)\left(\frac{\partial w}{\partial x} + \frac{\partial u}{\partial z}\right)\right] + \frac{\partial}{\partial y}\left[(\mu+\mu_t)\left(\frac{\partial w}{\partial y} + \frac{\partial v}{\partial z}\right)\right] + \frac{\partial}{\partial z}\left[(\mu+\mu_t)\left(\frac{\partial w}{\partial z} + \frac{\partial w}{\partial z}\right)\right]$$

Energy equation for the fluid region:

Table 1 The uncertainty of main parameters

Parameters	Formula	Maximum uncertainty
T	-	±0.20 °C
P	-	±0.08%
G	-	±0.5%
Re	$\frac{\triangle Re}{Re} = \sqrt{\left(\frac{\triangle u_m}{u_m}\right)^2 + \left(\frac{\triangle D_h}{D_h}\right) + \left(\frac{\triangle v}{v}\right)^2}$	±0.89%
h	$\frac{\triangle h}{h} = \sqrt{\left(\frac{\triangle Q}{Q}\right)^2 + \left(\frac{\triangle A_{ch}}{A_{ch}}\right) + \left(\frac{\triangle T_{hs}}{T_{hs}}\right)^2 + \left(\frac{\triangle T_m}{T_m}\right)^2}$	±5.63%
Nu	$\frac{\triangle Nu}{Nu} = \sqrt{\left(\frac{\triangle h}{h}\right)^2 + \left(\frac{\triangle D_h}{D_h}\right)^2 + \left(\frac{\triangle k_w}{k_w}\right)^2}$	±5.66%

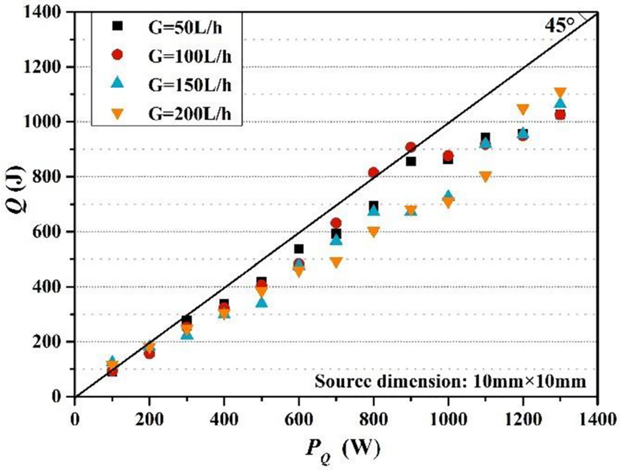

(a) Heat source dimension: 10 mm×10 mm.

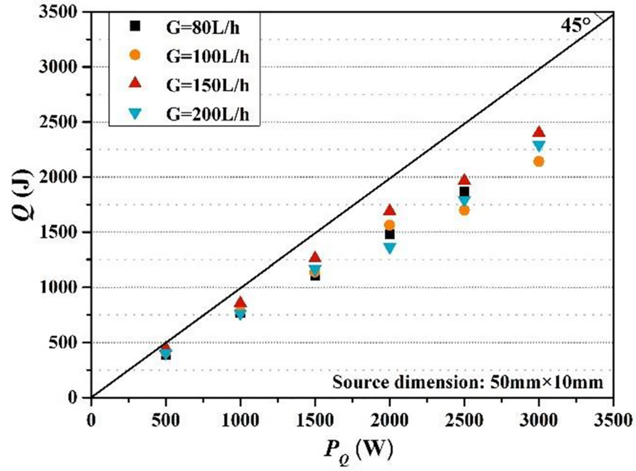

(b) Heat source dimension: 50 mm×10 mm.

Fig. 5 Thermal balance of specimens

$$\frac{\partial(\rho uT)}{\partial x}+\frac{\partial(\rho vT)}{\partial y}+\frac{\partial(\rho wT)}{\partial z}=\frac{\partial}{\partial x}\left[\left(\frac{\lambda_f}{c_p}+\frac{\mu_t}{\sigma_T}\right)\frac{\partial T}{\partial x}\right]+\frac{\partial}{\partial y}\left[\left(\frac{\lambda_f}{c_p}+\frac{\mu_t}{\sigma_T}\right)\frac{\partial T}{\partial y}\right]+\frac{\partial}{\partial z}\left[\left(\frac{\lambda_f}{c_p}+\frac{\mu_t}{\sigma_T}\right)\frac{\partial T}{\partial z}\right] \tag{15}$$

Energy equation for the solid region:

$$\frac{\partial}{\partial x}\left(\lambda_s\frac{\partial T}{\partial x}\right)+\frac{\partial}{\partial y}\left(\lambda_s\frac{\partial T}{\partial y}\right)+\frac{\partial}{\partial z}\left(\lambda_s\frac{\partial T}{\partial z}\right)=0 \tag{16}$$

In this study, the standard k-ε turbulence model was used to simulate the turbulent heat transfer. The governing equations of turbulence are given as follows.

$$\frac{\partial(\rho uk)}{\partial x}+\frac{\partial(\rho vk)}{\partial y}+\frac{\partial(\rho wk)}{\partial z}=\frac{\partial}{\partial x}\left[\left(\mu+\frac{\mu_t}{\sigma_k}\right)\frac{\partial k}{\partial x}\right]+\frac{\partial}{\partial y}\left[\left(\mu+\frac{\mu_t}{\sigma_k}\right)\frac{\partial k}{\partial y}\right]+\frac{\partial}{\partial z}\left[\left(\mu+\frac{\mu_t}{\sigma_k}\right)\frac{\partial k}{\partial z}\right]+G_k-\rho\varepsilon$$

$$\frac{\partial(\rho u\varepsilon)}{\partial x}+\frac{\partial(\rho v\varepsilon)}{\partial y}+\frac{\partial(\rho w\varepsilon)}{\partial z}=\frac{\partial}{\partial x}\left[\left(\mu+\frac{\mu_t}{\sigma_\varepsilon}\right)\frac{\partial \varepsilon}{\partial x}\right]+\frac{\partial}{\partial y}\left[\left(\mu+\frac{\mu_t}{\sigma_\varepsilon}\right)\frac{\partial \varepsilon}{\partial y}\right]+\frac{\partial}{\partial z}\left[\left(\mu+\frac{\mu_t}{\sigma_\varepsilon}\right)\frac{\partial \varepsilon}{\partial z}\right]+\frac{\varepsilon}{k}\left(c_1G_k-c_2\rho\varepsilon\right)$$

$$\mu_t=c_\mu\rho\frac{k^2}{\varepsilon}$$

$$G_k=\mu_t\left\{2\left[\left(\frac{\partial u}{\partial x}\right)^2+\left(\frac{\partial v}{\partial y}\right)^2+\left(\frac{\partial w}{\partial z}\right)^2\right]+\left(\frac{\partial u}{\partial y}+\frac{\partial v}{\partial x}\right)^2+\left(\frac{\partial u}{\partial z}+\frac{\partial w}{\partial x}\right)^2+\left(\frac{\partial v}{\partial z}+\frac{\partial w}{\partial y}\right)^2\right\} \tag{17}$$

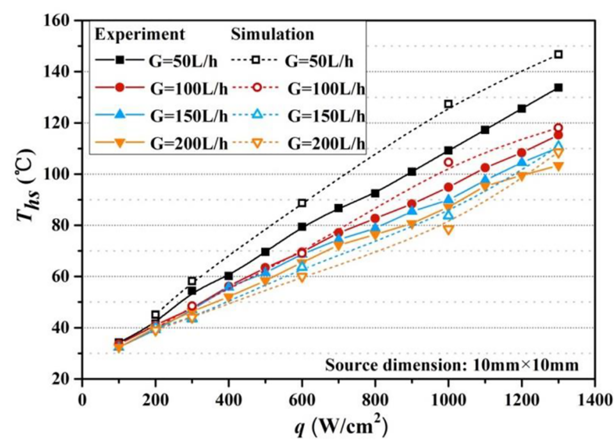

(a) Source dimension: 10mm×10mm

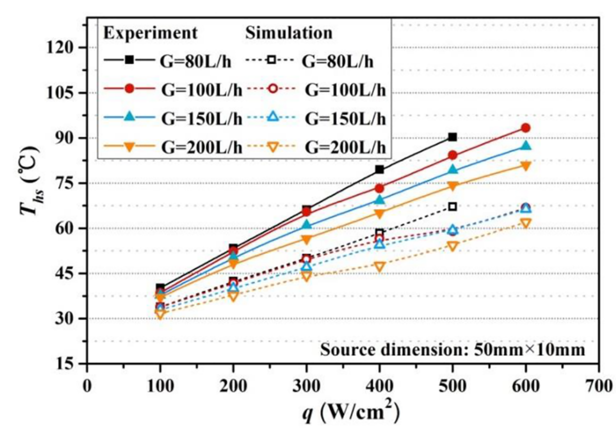

(b) Source dimension: 50mm×10mm

Fig. 6 Comparison of experimental results with numerical simulations of the junction temperature change with heat flux at different flow rates where λ *is* the thermal conductivity, μ_t represents the turbulent viscosity, c_μ, c_1, c_2, σ_k, σ_ε and σ_T equal to 0.09, 1.44, 1.92, 1.0, 1.3 and 0.9, respectively.

The meshing tool GAMBIT was used to mesh the computational domain of the microchannel heat sink, and computational fluid dynamics (CFD) software Fluent was used to solve the fluid flow and heat transfer numerically in the microchannel heat sink [40]. The momentum and energy conservation equations were discredited by a second-order upwind scheme. The SIMPLEC algorithm was adopted to deal with the relationship between velocity and pressure. The computations were considered to be converged when the

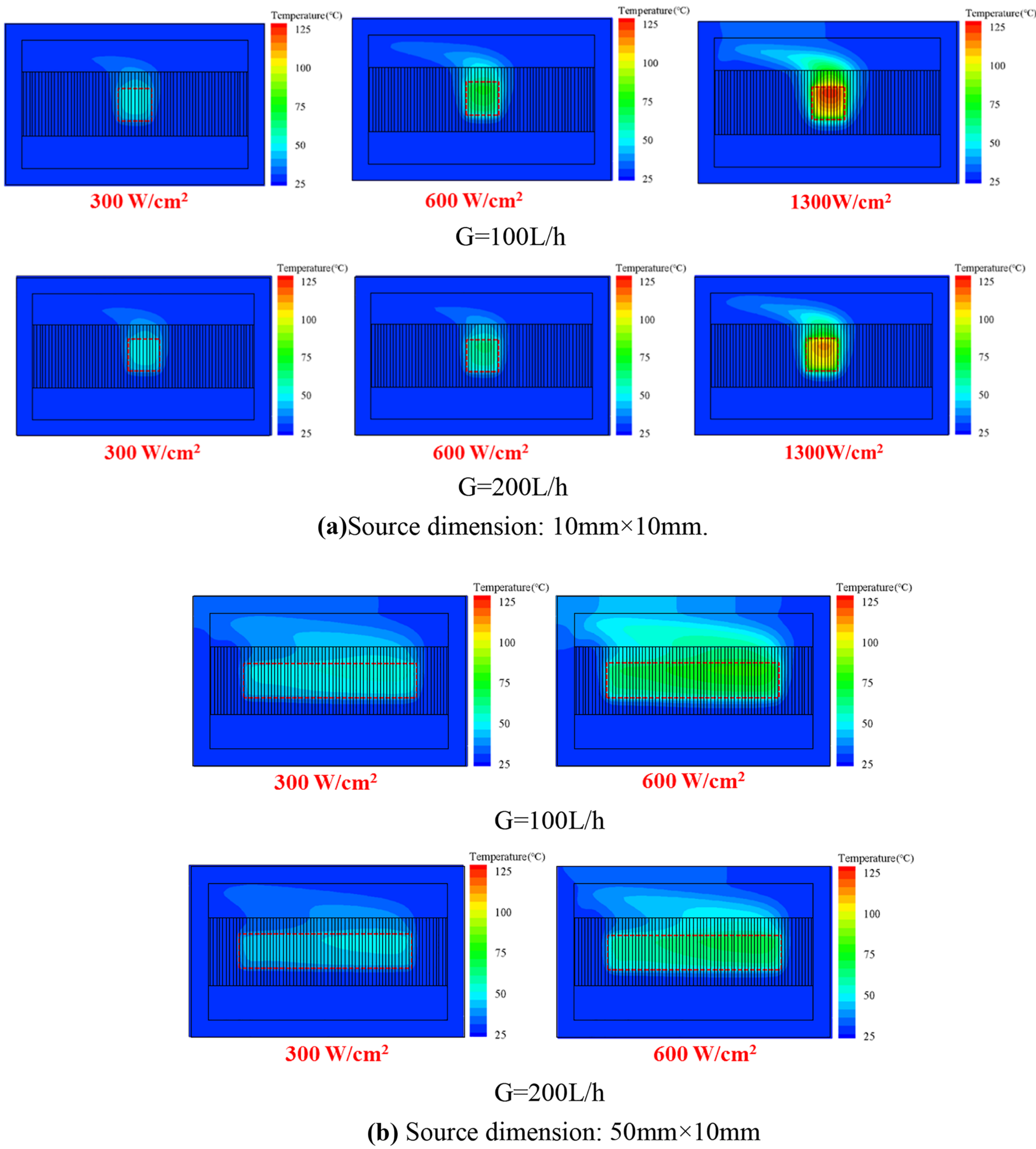

Fig. 7 Temperature clouds at the surface of the microchannel base plate

convergence residuals are less than 10^{-4} for the continuity and momentum equations and 10^{-6} for the energy equation.

The inlet was set as the velocity inlet, and the temperature was kept at 298.15 K. The outlet was set as pressure outlet and the relative pressure is 0 Pa. In addition, a heat source with a constant heat flux was applied to the bottom of the microchannel heat sink, as shown in Fig. 2, and the other walls were assumed to be thermally insulated. Copper with thermal conductivity of 387.6 W/(m•K) was chosen as the material for the microchannel heat sink, and liquid water with temperature dependent thermophysical properties [41] was used as the heat transfer fluid.

The grid independence study was carried out based on the microchannel heat sink model with three grid densities (1,205,151 cells, 2,671,119 cells and 3,586,719 cells). The deviations in ΔP and T_{hs} between the 2,671,119 cells and 3,586,719 cells are 0.33% and 0.12%, respectively. This indicates that the calculation with grid densities of 2,671,119 cells is accurate enough. Therefore, all the computations were carried out using the mesh with 2,671,119 cells considering both computational accuracy and efficiency.

5 Experiment results and discussion

5.1 Energy balance calibration

As shown in the Fig. 5(a), (b), the heat input from the AC power supply was compared with the heat carried away by the coolant water. The value calculated by Eq. (6) is lower than that of the power input of AC power supply from Eq. (5), indicating that there exists heat loss. As the input heat increased from 100 to 1300 W and 3000 W respectively, this deviation became more obvious, ranging from 10 to 30%. According to Eq. (6), the highest heat flux values achieved in the experiments were actually 1104.54 W/cm^2 and 480.60 W/cm^2 for the heat source areas of 1cm^2 and 5cm^2, respectively. The heat loss is mainly composed of two parts: the first part is the heat loss caused by the measurement error of temperature and flow rate; the second part of the thermal leakage, which occupied the main part, is caused by convection and radiant heat transfer on the surface of the heating block. During the experiment, as the input power increased, a large temperature gradient was generated on the surface of the heating block. For example, when the input power of the AC power supply was 1000 W, the maximum temperature of the copper block surface can reach 500 °C, which exceeded the melting point of the thermal insulation cotton. Insulation material will deform and produce large amounts of fumes when overheated, which is detrimental to the proper functioning of the heat source.

5.2 Hydraulic and heat transfer characteristics

The junction temperature T_{hs} of the heating source at different flow rate are plotted against heat fluxes in Fig. 6(a) ,(b), respectively. In Fig. 6(a), it is showed that the temperature increased linearly with the input heat flux increasing from 100 W/cm^2 to 1300 W/cm^2 with heat source dimension of 1cm^2. Taking 85 °C as the upper limit of junction

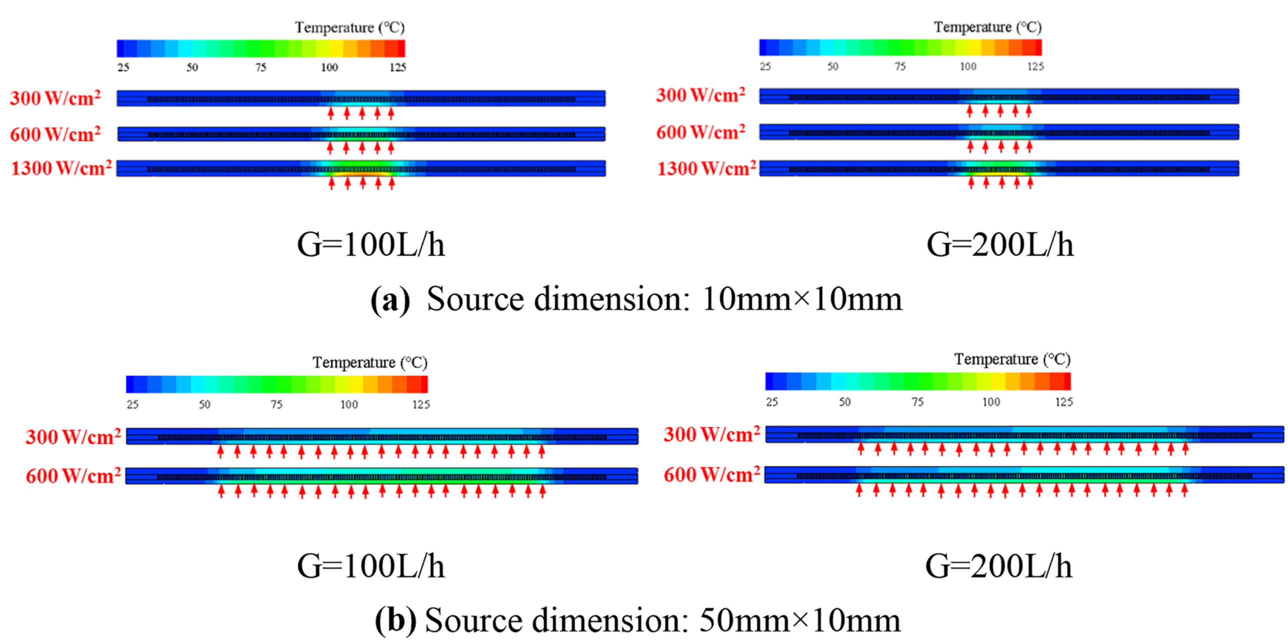

Fig. 8 Temperature cloud plots of cross sections in the length direction (y direction) for two heat source areas

temperature for normal operation of electronic equipment, the structure proposed in this paper dissipated heat flux greater than 1000 W/cm^2 at the flow rate of 200L/h, which means that the suggested heat sink can realize the thermal management of heat flux of 1000 W/cm^2 without overheating.

In addition, it can be seen from the Fig. 6(a) that under the same heat load, the T_{hs} decreased as the flow rate increased, especially at high heat flux. With a gradual increased in flow rate from 50L/h to 200L/h, the junction temperature was 109.20 ºC, 94.85 ºC, 89.90 ºC and 87.15 ºC at the heat flux of 1000 W/cm^2, and the temperature decrease ratio was 13.14%, 5.22% and 3.06%, respectively.

Figure 6(a) also exhibits the comparison between the experimental results and numerical simulations of the junction temperature variation with heat flux. It can be seen from the figure that the trend of temperature change is almost the same. At smaller flow rates that below 100 L/h, a large difference occurred when the heat flux exceeded 700 W/cm^2. This may be due to the unavoidable leakage of heat from the heating block during the experiment making the actual input heat density lower than the uniform heat flux in the simulation. From the temperature cloud diagram of the microchannel base plate as given in Fig. 7(a), it can be observed that at higher heat flux, the temperature of the heat source region will gradually decrease along the flow direction as the flow rate increases. However, during the experiment, the junction temperature was measured at the top of the heating block, and there was a thin layer of solder paste between the microchannel heat sink base plate and the heating block. This means that there was an additional thermal resistance between the temperature measurement point and the heat sink base plate, which slightly weaken the heat transfer. In addition, as can be seen in Fig. 8(a) the heat flux was uniformly input during the simulation and the effect of solder paste on heat transfer was not considered. Therefore, at high flow rates, the simulation results of junction temperature are lower than the experimental results.

Variations of the junction temperature with heat flux for the heating source of 5cm^2 are shown in Fig. 6(b). At a constant flow rate, the junction temperature increased linearly with the increases in heat flux. When the input heat flux increased from 100 W/cm^2 to 600 W/cm^2, the junction temperature rose from 38.57 °C to 93.33 °C at the flow rate of 100L/h. Also, under all operating conditions, the T_{hs} was less than 100 °C. When the flow rate gradually increased from 80L/h to 200L/h, the T_{hs} dropped significantly, and the decline slope was basically the same, about 6%. This result indicated that increasing the flow rate within the allowable range could reduce the overall temperature of the heat sink and enhance the heat transfer performance.

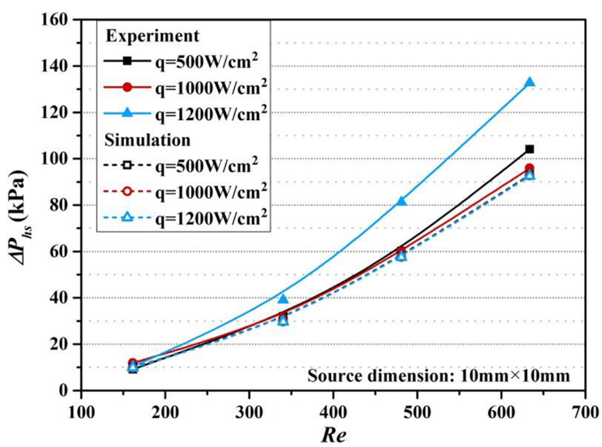

(a) Source dimension: 10mm×10mm

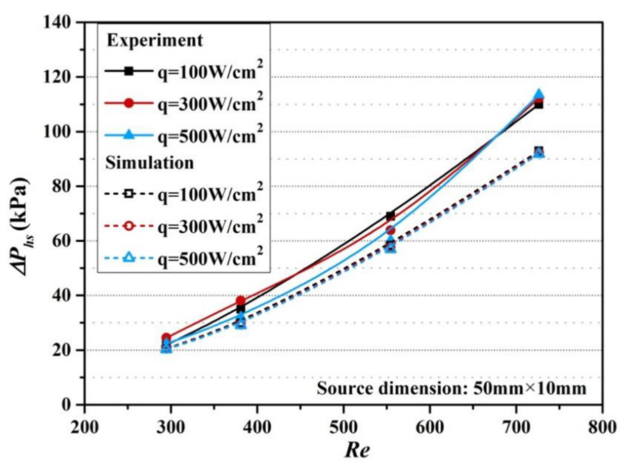

(b) Source dimension: 50mm×10mm

Fig. 9 Comparison of experimental and numerical simulation results regarding the pressure drop of heat sink

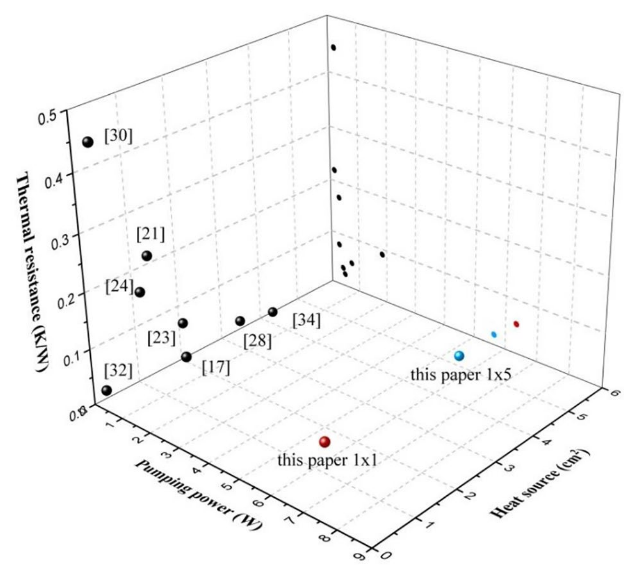

Fig. 10 Summary and comparison of the published experimental results and ours

Table 2 Comparison of published experimental results in Fig. 10

Years	Author	D_h (μm)	Channel types	Material	Loop form	Coolant	Pressure drop (kPa)	Flow rate (ml/min)	T_{in} (℃)	Heat flux (W/cm^2)	Heat source area (cm^2)	Thermal resistance (K/W)	Re	Pumping power (W)
1981	Tuckerman and Pease [17]	85–95	Rectangular	Silicon	NA	Water	213.745	282–516	23	181–790	1 × 1	0.09	NA	1.84
2005	Chang et al. [21]	100–225	Rectangular	Silicon	Closed	DI water	< 57.7	159	NA	1250	1 × 1.3	0.22	NA	0.15
2006	Solovitz et al. [23]	NA	Trapezoidal	Copper	Closed	DI water	< 68.95	240	20	104	1.92	0.078	NA	0.28
2007	Colgan et al. [28]	96, 106	Staggered and continuous fins	Silicon	Closed	Water	< 35	NA	22	400	3	0.05	NA	0.73
2008	Brunschwiler et al. [24]	182, 333	Rectangular pin fin	Silicon	NA	DI water	< 70	< 400	25	200	1	0.17	< 1000	0.30
2010	Escher et al. [25]	46–158	Rectangular	Silicon	Closed	Water	22	1300	20	100	2 × 2	0.022	NA	0.48
2015	Xia et al [30]	150, 240	Straight and corrugated channel	Silicon	Closed	DI water	< 65	75–190	25	200	0.4 × 0.6	0.446	250–611	0.21
2019	Zhang et al. [32]	1667	Rectangular	Copper	Closed	Galinstan	8	1200–4800	27	300	0.22 × 0.22	0.034	2481	0.41
This paper		320	Rectangular	Copper	Closed	DI water	< 133.48	833–3333	25	1104.54	1 and 5	0.065 and 0.019	150–750	0.1–6.5

Figure 6(b) also shows a comparison of the experimental and numerical results for junction temperature. Figures 7(b) and 8(b) shows the results of the numerical simulation of the temperature cloud plots. As can be seen from the figure, the values of the experimental results are higher than those of the simulations, and the deviation of the temperature increases with the increase of the heat flux. The reason for this phenomenon may be that the uneven solder paste used to connect the heat sink to the heating block caused a large resistance to heat transfer, especially at large heat source areas. In addition, the uniform heat flux was used as a heat source boundary condition in the numerical simulations and the effect of the solder paste on the heat transfer was not taken into account. If we adjust the thickness of the solder in the model, this discrepancy will be reduced. It can be predicted from the simulation results that the microchannel heat sink proposed in this paper can achieve better cooling performance at high heat flux and large heat transfer area if the influence of contact thermal resistance can be reduced.

The pressure drop of microchannel heat sink versus *Re* number under different heat flux are illustrated in Fig. 9(a) and (b). As can be seen from the Fig. 9(a), the pressure drop of the heat sink and its rising rate increased with Reynolds number under the experimental conditions. The largest pressure drop of 133.48 kPa was recorded at $q=1200$ W/cm^2 and $Re=667$. In addition, for the same number of *Re*, the pressure drop had a slight fluctuation with the increase in heat flux. This may due to the fact that the viscosity of the water was strongly influenced by temperature, and when the heat flux was increased, the water temperature became higher, the viscosity decreased, and Re increased, resulting in changes in the coefficient of friction and pressure drop.

In Fig. 9(b), since the main structure and the channel size of the heat sink for two heating source scenarios are the same, the pressure drop of heat sink is of the same order of magnitude. The overall trend was that the pressure drop increased with increasing of *Re*. The maximum value of pressure drop was 114.87 kPa when the $q=500$ W/cm^2 and $Re=726$.

Figure 9(a), (b) also compared the experimental and numerical results of microchannel pressure drop. As can be seen in the figures, there is some deviation between the two results and the experimental results are slightly larger than the simulated results. There are three possible reasons for this discrepancy: (1) this is a simplified model, as shown in Fig. 4, and the influence from some obstacles (e.g. sensors) was not considered; (2) the standard k-ε turbulence model might not match the real situation perfectly; (3) the measurement errors of the pressure sensors will affect the results. During the simulation process, both the channel and the fluid were in the ideal state, so the simulation results were lower than the experimental results.

5.3 The relationship of thermal resistance and pumping power for two heating scenarios

Under the maximum input heat flux of 1300 W/cm^2 and flow rate of 200L/h, the total thermal resistance was 0.065 K/W for 1cm^2 heat source. The lowest value of the thermal resistance was 0.019 K/W for 5cm^2 heat source at the input heat flux of 600 W/cm^2 and the flow rate of 200L/h. When the heat source area increased from 1cm^2 to 5cm^2, the thermal resistance value decreased significantly, which is due to the lower input heat flux. When the unit is converted to K•cm^2/W, the thermal resistance value of the two different heat transfer area is the consistent.

Figure 10 and Table 2 summarizes the comparison of some published experimental results for different heat source area, pumping power, and thermal resistance in the historic literature which were aiming at solving high heat flux, and the results in this work are also marked in the figure using red and blue dots. It is obvious from the diagram that the turbulence-enhanced and structure-optimized microchannel proposed in this paper achieves an unprecedented ultra-low thermal resistance for a large heat transfer area with a very high heat flux, consuming only 6 W of pumping power.

6 Conclusive remarks

In order to explore the heat transfer potential of microchannel heat sinks for high heat flux cooling, a structure-optimized microchannels, with 0.2 mm width, 0.8 mm height, were experimentally and numerically studied under different heat flux and flow rate. A carefully designed cooling circulation system has been proposed to meet the heat dissipation requirements of high heat flux. The inlet and outlet temperature, pressure drop and flow rate of coolant are measured under different heat loads in this work. The experimental and simulation result indicates that the proposed copper-based microchannel thermal management system can dissipate heat flux of 1000 W/cm^2 over 1 cm^2 and 500 W/cm^2 over 5 cm^2, respectively. In addition, extremely low thermal resistance of 0.065 K/W and 0.019 K/W were obtained for these two heating area scenarios. Overall, the proposed copper-based optimized microchannel heat sink is a practical and efficient cooling method that promises to be used for large-scale and high heat flux equipment. In future work, modifications to the structure of proposed heat sink, such as a manifold layout or porous surface coating, can be considered to achieve heat dissipation with ultra-high heat flux.

Acknowledgements This work is supported by the National Natural Science Foundation of China (Project No.51776195).

References

1. Mudawar I (2001) Assessment of high-heat-flux thermal management schemes. IEEE Trans Compon Packag Technol 24(2):122–122
2. Bar-Cohen A, Wang P, Rahim E (2007) Thermal management of high heat flux nanoelectronic chips. Microgravity Sci Technol 19(3):48–52
3. Lee J, Mudawar I (2008) Fluid flow and heat transfer characteristics of low temperature two-phase micro-channel heat sinks – Part 1: Experimental methods and flow visualization results. Int J Heat Mass Transf 51:4315–4326
4. Lasance CJM, Poppe A (2014) Thermal Management for LED Applications New York
5. Habibi Khalaj A, Halgamuge SK (2017) A review on efficient thermal management of air- and liquid-cooled data centers: From chip to the cooling system. Appl Energy 205:1165–1188
6. Karayiannis TG, Mahmoud MM (2017) Flow boiling in microchannels: Fundamentals and applications. Appl Therm Eng 115:1372–1397
7. Dix J, Jokar A (2010) Fluid and thermal analysis of a microchannel electronics coolerusing computational fluid dynamics. Appl Therm Eng 30(8):948–961
8. Kadam ST, Kumar R (2014) Twenty first century cooling solution: microchannelheat sinks. Int J Therm Sci 85:73–92
9. Agostini B, Fabbri M, Park JE, Wojtan L, Thome JR, Michel B (2007) State of the artof high heat flux cooling technologies. Heat Transfer Eng 28:258–281
10. Reddy SR, Dulikravich GS (2015) Multi-objective optimization of micro pin-fin arrays for cooling of high heat flux electronics. in: Proc IMECE2015. Texas
11. Yeh LT (1995) Review of heat transfer technologies in electronicequipment. ASME J Electron Packag 117:333–339
12. Ebadian MA, Lin CX (2011) A review of high-heat-flux heat removal technologies. J Heat Trans 133(11):112–112
13. Christensen A, Graham S (2009) Thermal effects in packaging high power light emitting diode arrays. Appl Therm Eng 29:364–371
14. Gilmore N, Timchenko V, Menictas C (2018) Microchannel cooling of concentrator photovoltaics: A review. Renew Sustain Energy Rev 90:1041–1059
15. Kandlikar SG, Grande WJ (2003) Evolution of microchannel flow passages-thermohydraulic performance and fabrication technology. Heat Transfer Eng 24:13–17
16. Khan MG, Fartaj A (2011) A review on microchannel heat exchangers and potential applications. Int J Energy Res 35:553–582
17. Tuckerman DB, Pease RFW (1981) High-performance heat sinking for VLSI. IEEE Electron Device Lett 2:126–129
18. Naterer GF (2005) Reducing energy availability losses with open parallel microchannels embedded in a micropatterned surface. Int J Energy Res 29:1215–1229
19. Skidmore JA, Freitas BL, Crawford J, Satariano J, Utterback E, DiMercurio L, Cutter K, Sutton S (2000) Silicon monolithic microchannel-cooled laser diode array. Appl Phys Lett 77(1):10–12
20. Qu W, Mudawar I (2002) Experimental and numerical study of pressure drop and heat transfer in a single-phase micro-channel heat sink. Int J Heat Mass Transf 45:2549–2565
21. Chang JY, Prasher RS, Chau D, Myers A, Dirner J, Prstic S, He D (2005) Convective performance of package based single phase microchannel heat exchanger. in: Proc IPACK2005. San Francisco
22. Hirshfeld H, Silverman I, Arenshtam A, Kijel D, Nagler, (2006) A High heat flux cooling of accelerator targets with micro-channels. Nucl Instrum Methods Phys Res Sect A: Accelerators Spectrometers Detectors Associated Equipment 562(2):903–905
23. Solovitz SA, Stevanovic LD, Beaupre RA (2006) Micro-channel thermal manage-ment of high power devices. in: Applied Power Electronics Conference and Exposition. Dallas
24. Brunschwiler T, Michel B, Rothuizen H, Kloter U, Wunderle B, Oppermann H (2008) Forced Convective Interlayer Cooling in Vertically Integrated Packages. in: Proc ITherm. Orlando
25. Escher W, Brunschwiler T, Michel B, Poulikakos D (2010) Experimental investigation of an ultra-thin manifold microchannel heat sink for liquid-cooled chips. J Heat Transfer 132 (8):081402
26. Koyuncuoğlu A, Jafari R, Okutucu-Özyurt T, Külah H (2012) Heat transfer and pressure drop experiments on CMOS compatible microchannel heat sinks for monolithic chip cooling applications. Int J Therm Sci 56:77–85
27. Kozłowska A, Łapka P, Seredyński M, Teodorczyk M, Dąbrowska-Tumańska E (2015) Experimental study and numerical modeling of micro-channel cooler with micro-pipes for high-power diode laser arrays. Appl Therm Eng 91:279–287
28. Colgan EG, Furman B, Gaynes M, Graham W, LaBianca N, Magerlein JH, Polastre RJ, Rothwell MB (2007) A practical implementation of silicon microchannel coolers for high power chips. IEEE T Compon Pack T 30(2):218–225
29. Lee YJ, Lee PS, Chou SK (2013) Hotspot mitigating with obliquely finned microchannel heat sink–an experimental study. IEEE Trans Compon Packag Technol 3:1332–1341
30. Xia GD, Ma DD, Zhai YL, Li YF, Liu R, Du M (2015) Experimental and numerical study of fluid flow and heat transfer characteristics in microchannel heat sink with complex structure. Appl Therm Eng 105:848–857
31. Liu HL, An XK, Wang CS (2017) Heat transfer performance of T-Y type micro-channel heat sink with liquid GaInSn coolant. Int J Therm Sci 120:203–219
32. Zhang XD, Yang XH, Zhou YX, Rao W, Gao JY, Ding YJ, Shu QQ, Liu J (2019) Experimental investigation of galinstan based minichannel cooling for high heat flux and large heat power thermal management. Energ Convers Manage 185:248–258
33. Shamim MS, Narde RS, Gonzalez-Hernandez JL, Ganguly A, Venkatarmanb J, Kandlikar SG (2019) Evaluation of Wireless Network-on-Chip Architectures with Microchannel-Based Cooling in 3D Multicore Chips. Sustain Comput Infor 21:165–178
34. Xie H, Yang B, Zhang SY, Song MR (2020) Research on the mechanism of heat transfer enhancement in microchannel heat sinks with micropin fins. Int J Energy Res 44(9):1–17
35. Yang M, Cao BY (2020) Multi-objective optimization of a hybrid microchannel heat sink combining manifold concept with secondary channels. Appl Therm Eng 181:115592
36. Erp RV, Soleimanzadeh R, Nela L, Kampitsis G, Matioli E (2020) Co-designing electronics with microfluidics for more sustainable cooling. Nature 585:211–216
37. Hu JS, Zuo GZ, Maingi R et al (2019) Experiments of continuously and stably flowing lithium limiter in EAST towards a solution for the power exhaust of future fusion devices. Nucl Mater Energy 18:99–104
38. Li J, Peterson GP (2007) 3-Dimentional Numerical Optimization of Silicon-based High Performance Parallel-channel Micro Heat Sink with Liquid Flow. Int J Heat Mass Transf 50:2895–2904
39. Li J, Peterson GP (2006) Geometric Optimization of an Integrated Micro Heat Sink with liquid Flow. IEEE Trans Components and Packaging Technologies 29:145–154
40. ANSYS FLUENT Tutorial Guide 19.2
41. Incropera FP (1999) Liquid Cooling of Electronic Devices by Single-Phase Convection. Wiley-Interscience